This document is the accepted manuscript version of the following article:
Luo, Z., Dao, P. T., Hrabec, A., Vijayakumar, J., Kleibert, A., Baumgartner, M., … Gambardella, P. (2019). Chirally coupled nanomagnets. Science, 363(6434), 1435-1439. https://doi.org/10.1126/science.aau7913

Title: Chirally Coupled Nanomagnets

Authors: Zhaochu Luo[1,2*], Trong Phuong Dao[1,2,3], Aleš Hrabec[1,2,3], Jaianth Vijayakumar[2], Armin Kleibert[2], Manuel Baumgartner[3], Eugenie Kirk[1,2], Jizhai Cui[1,2], Tatiana Savchenko[2], Gunasheel Krishnaswamy[3], Laura J. Heyderman[1,2*], Pietro Gambardella[3*].

Affiliations:

[1]Laboratory for Mesoscopic Systems, Department of Materials, ETH Zurich, 8093 Zurich, Switzerland.

[2]Paul Scherrer Institut, 5232 Villigen PSI, Switzerland.

[3]Laboratory for Magnetism and Interface Physics, Department of Materials, ETH Zurich, 8093 Zurich, Switzerland.

*Correspondence to: zhaochu.luo@psi.ch (Z.L.); laura.heyderman@psi.ch (L.H.); pietro.gambardella@mat.ethz.ch (P.G.).

Abstract: Magnetically coupled nanomagnets have multiple applications in non-volatile memories, logic gates, and sensors. The most effective coupling has been found to occur between the magnetic layers in a vertical stack. Here we achieve strong coupling of laterally adjacent nanomagnets employing the interfacial Dzyaloshinskii-Moriya interaction. This coupling is mediated by chiral domain walls between out-of-plane and in-plane magnetic regions and dominates the behavior of nanomagnets below a critical size. We utilize this concept to realize lateral exchange bias, field-free current-induced switching between multistate magnetic configurations, as well as synthetic antiferromagnets, skyrmions, and artificial spin ices covering a broad range of length scales and topologies. Our work provides a platform to achieve all-electric control of planar logic gates and memory devices.

Main Text:

Engineering the coupling between magnetic elements is central to fundamental advances in magnetism and spintronics. The discovery of interlayer coupling between two ferromagnetic layers separated by a non-magnetic spacer, caused by the Ruderman-Kittel-Kasuya-Yosida interaction, has led to the realization of synthetic antiferromagnets (*1-3*) and the discovery of giant magnetoresistance (*4,5*). Similarly, the exchange bias between ferromagnetic and antiferromagnetic layers (*6*) is widely employed to stabilize the magnetic reference layer in spin valves and magnetic tunnel junctions (*7,8*). These couplings are highly effective in vertically stacked structures. However, in order to realize two-dimensional networks of nanoscale magnetic elements, it is desirable to engineer effective lateral couplings in a controllable way. So far, this has been achieved by exploiting long-range dipolar interactions (9-12). However, the dipolar interaction is non-local and scales inversely with the volume of the magnets, which limits its use in applications involving nanometer sized structures and thin films.

Here, we demonstrate an alternative mechanism to control the lateral coupling between adjacent magnetic nanostructures. Our concept is based on the interfacial Dzyaloshinskii-Moriya interaction (DMI), $H_{\mathrm{DM}} = -\boldsymbol{D}_{ij}\cdot(\boldsymbol{m}_i \times \boldsymbol{m}_j)$, which embodies the anti-symmetric exchange coupling between two neighboring magnetic moments $\boldsymbol{m}_i$ and $\boldsymbol{m}_j$ induced by the spin-orbit interaction in a structurally asymmetric environment (*13,14*). In contrast to the symmetric exchange interaction, which favors a parallel alignment of the magnetic moments, the DMI favors an orthogonal orientation of $\boldsymbol{m}_i$ relative to $\boldsymbol{m}_j$, with a fixed chirality given by the direction of the Dzyaloshinskii-vector $\boldsymbol{D}_{ij}$. At the interface between a magnetic layer and a heavy metal, the DMI can be strong enough to induce the formation of noncollinear spin textures such as spin spirals (*15*) and skyrmions (*16,17*). Often, however, the competition between the DMI, the exchange

interaction, and the magnetic anisotropy in thin films with out-of-plane (OOP) magnetization results in the formation of chiral domain walls separating large regions with uniform up or down magnetic moments (*18,19)*. In these systems, the DMI also plays a crucial role in determining the direction and speed of current-induced domain wall motion (*20-23*). Here we exploit the DMI to control the lateral coupling between OOP and in-plane (IP) magnetic structures (Fig. 1A) and demonstrate unique phenomena associated with such chirally coupled nanomagnets.

We fabricated arrays of nanomagnets that combine strong DMI with regions exhibiting IP and OOP magnetic anisotropy. Pt(6 nm)/Co(1.6 nm)/AlO_x trilayers were patterned by electron beam lithography and Ar ion milling (*24*). Here AlO_x refers to an Al layer that is oxidized in an oxygen plasma. Such magnetic trilayers have a large DMI (*25,26*) as well as tunable magnetic anisotropy, which is IP or OOP depending on the degree of oxidation of the Co/Al interface (*27*, Fig. S1), and are widely used as a model system for studying current-induced switching and domain wall motion in spintronic devices (*28,29*). A scanning electron micrograph of an array of Co elements, each consisting of adjacent IP and OOP regions is given in Fig. 1B. The size and shape of the IP magnetized region is controlled by covering the Al with a thin Ta protective layer to prevent oxidation during the oxygen plasma process.

X-ray photo-emission electron microscopy (X-PEEM) images provide first evidence that the magnetizations of the OOP and IP regions are coupled, and that this coupling is chiral. Figure 1C shows that if the magnetization of the IP region points to the right ("→"), following saturation with an in-plane magnetic field, OOP regions on the left and right of the IP region point down ("↓") and up ("↑"), respectively. The relative orientation between OOP and IP parts is thus either ↓→ or →↑, which agrees with the left-handed chirality expected from the negative

sign of the DMI in Pt/Co/AlO_x (*25*). As expected, reversing the direction of the in-plane field leads to the observation of ↑← and ←↓ coupling (Fig. S8).

To further analyze the chiral coupling between OOP and IP regions, we measured the anomalous Hall resistance of OOP-IP Co/AlO_x elements fabricated on top of a Pt Hall cross (Fig. 1D) as a function of external magnetic field. As the anomalous Hall effect is proportional to the *z*-component of the magnetization, these measurements reflect the state of the OOP region, with the IP magnetization pre-set by an in-plane field applied parallel to *y*. For an external field H_{ext} // *z*, we find that the hysteresis loop of the OOP region shifts by more than 200 Oe towards positive or negative field for right or left orientation of the IP magnetization, respectively (Fig. 2A). These opposite shifts indicate that the DMI strongly favors the ↓→ and ↑← configurations, resulting in an effective exchange bias field H_{bias}, whose sign can be tuned by pre-setting the orientation of the IP magnetization. Hence, the chiral coupling demonstrated here provides a method to realize large hysteresis bias in lateral structures

When the external field is applied in-plane, H_{ext} // *y*, we additionally find that the OOP region switches direction simultaneously with the IP region (Fig. 2B, 2C and S3). Starting from the DMI-stable ↑← configuration, the OOP region switches from up to down as the in-plane field switches the IP magnetization from ← to →, thus avoiding the unfavorable ↑→ configuration. This observation implies that the energy associated with the chiral coupling is larger than the energy of the barrier to switch the OOP region, so that the direction of the IP magnetization effectively controls the OOP magnetization. If the applied magnetic field is tilted in the *y*-*z* plane, the field can also induce the switching of the OOP region, which then biases the IP magnetization. Therefore, depending on the coercivity of the OOP and IP regions and on the tilt angle θ of the external field, we observe switching between different multistate magnetic

configurations (Fig. 2B). If both the out-of-plane and in-plane field components of the applied magnetic field assist the DMI-favored configurations, we observe bistable switching between the ↓→ and ↑← states (Type I behavior, similar to H_{ext} // y). In contrast, if the two field components prefer the DMI-unfavored ↓← and ↑→ configurations, we observe switching between all the four possible combinations of states, with the sequence determined by the relative amplitude of the in-plane and out-of-plane magnetic field components (Type II and Type III behavior).

The switching of the OOP-IP elements can be modeled with two coupled OOP and IP macrospins (*24*), where the energy of each configuration ($E_{\uparrow\rightarrow}$, $E_{\downarrow\rightarrow}$, $E_{\uparrow\leftarrow}$ and $E_{\downarrow\leftarrow}$) is given by the sum of the Zeeman energy and the energy associated with the DMI between the magnetic moments of the OOP and IP regions, $\boldsymbol{M}_{OOP}$ and $\boldsymbol{M}_{IP}$: $E = -(\boldsymbol{M}_{OOP} + \boldsymbol{M}_{IP})\cdot\boldsymbol{H}_{ext} - \boldsymbol{D}\cdot(\boldsymbol{M}_{OOP} \times \boldsymbol{M}_{IP})$. Assuming that the OOP (IP) magnetization switches whenever the energy difference between two configurations is larger than the energy barrier for magnetization reversal ΔE_{OOP} (ΔE_{IP}), the critical switching fields for the OOP and IP regions are given by $H^*_{z\pm} = (\Delta E_{OOP} \pm E_{DM})/2M_{OOP}$ and $H^*_y = (\Delta E_{IP} + E_{DM})/2M_{IP}$, respectively, where E_{DM} is the chiral coupling energy. As expected from the model, the switching fields of the OOP region determined experimentally lie on horizontal and vertical lines of an H_z-H_y diagram (Fig. 2D). We therefore identify these lines as the critical fields $H^*_{z\pm}$ and H^*_y. From these data, we determine the value of E_{DM} = 3.5 ±0.3 eV and the DMI constant D = -0.9 ±0.1 mJ/m^2, which is in good agreement with previous estimates of the DMI in Pt/Co/AlO$_x$ (*25*).

As E_{DM} is proportional to the length l_x of the quasi-1D domain wall separating the OOP and IP regions, whereas ΔE_{OOP} is proportional to the area $l_x w$, where w is the width of the OOP region (Fig. 2E, inset), the ratio $E_{DM}/\Delta E_{OOP} \propto 1/w$ increases when decreasing the dimensions of

the element. Hence, below a critical size, the magnetic behavior of the OOP region is predominantly determined by the chiral coupling. The boundaries that delimit this region are defined by $E_{DM}/\Delta E_{OOP} > 1$ and the single domain condition $w < w_{SD} \propto \sqrt{H_K}$, where w_{SD} and H_K are the critical single domain dimension and the OOP effective anisotropy field, respectively. These boundaries are shown in Fig. 2E together with the results of micromagnetic simulations that provide additional support to our model (*24* and Fig. S10). A similar reasoning can be applied to model the influence of the OOP magnetization on the IP magnetization taking into account that the IP anisotropy is shape-dependent. The favorable scaling of $E_{DM}/\Delta E_{OOP}$ and $E_{DM}/\Delta E_{IP}$ towards reduced dimensions means that chiral coupling can be exploited to control the magnetization of small systems. In our case the thermal stability factor is $E_{DM}/k_BT \approx 140$ at room temperature, so the width w of the patterned element can be reduced down to 35 nm while retaining a thermal stability larger than 40 k_BT.

We now illustrate possible applications of chiral coupling. First we discuss the fabrication of tailor-made laterally coupled synthetic antiferromagnetic structures, skyrmions, and artificial spin systems. As a starting point, we consider two separate OOP regions that are coupled by an IP spacer. X-PEEM imaging reveals that the static orientation of two OOP elements connected by an IP spacer is antiparallel and that, if the IP magnetization is pre-set with a magnetic field to the right, the OOP-IP-OOP magnetization is ↓→↑ (Fig. 3, A and B), in agreement with the left-handed chirality imposed by the DMI. The behavior of these structures was characterized by their anomalous Hall resistance in an applied field (Fig. 3C). To differentiate the two OOP regions, one side was made smaller than the other. For $H_{ext} \parallel z$, the flat curve between the two shifted hysteresis loops in Fig. 3C indicates that the OOP regions are coupled antiparallel at low field, whereas the parallel orientation can only be enforced by magnetic fields larger than 400-

600 Oe. The ↑↓ and ↓↑ antiferromagnetic states at zero magnetic field are set by pre-aligning the IP magnetization to be ← or →, respectively. Notably, the antiferromagnetic state at zero field is achieved independently of the initial orientation and amplitude of the field. Similar to the OOP-IP element, all the possible combinations of states 1-6 shown in Fig. 3C can be reached by changing the direction of the field in the *y*-*z* plane (Fig. 3D).

As long as the IP spacer retains a monodomain state, the two OOP elements effectively interact with each other. Thus, reversing the magnetization of one OOP element with a field H_{ext} // *z* causes the reversal of the IP spacer and subsequently the reversal of the other OOP element. In addition, magnetic force microscopy (MFM) measurements (Fig. 3E) demonstrate that the effective antiferromagnetic coupling between the OOP elements is a function of the IP spacer length l_y, leading to correlated reversal events for l_y < 300 nm and a nearly 100 % correlated switching probability for $l_y \leq 50$ nm. These measurements are performed on structures including two OOP elements with different sizes, such that the largest (smallest) element switches with (against) the external field H_z. OOP-IP-OOP structures with $l_y > 1$ μm (Fig. S11A) and curvilinear geometries (Fig. S11C) also have alternate up and down magnetized OOP regions. However, in such cases, the IP regions might assume a multidomain configuration and can effectively be replaced by two separate IP connectors. These two short sections can then be used to control the OOP magnetization in a nonlocal way. For all these structures, we find that the effective antiferromagnetic interaction mediated by chiral coupling is orders of magnitude stronger than the dipolar coupling between magnets of the same size and separation (Fig. S6).

Coupled OOP and IP elements can be further used as building blocks of more complex spin systems having a well-defined symmetry and topology. In Fig. 3F, a linear chain consisting of five OOP and IP regions is shown with alternating OOP magnetic moments. Such a structure can

be used to propagate magnetic information from one end of the chain to the other. Synthetic Néel skyrmions can also be realized by the coupling between concentric OOP rings via 50 nm wide circular IP spacers (Fig. 3G). By patterning more IP rings, we can create skyrmionic structures that do not have a counterpart in unpatterned thin films, with a topological charge that alternates between +/-1 and 0 (so-called skyrmioniums or target skyrmions) depending on the number of rings. Such structures might be of interest to study high-frequency excitations of skyrmions, as well as for the generation and transmission of spin waves in magnonic crystals. Finally, strongly coupled artificial spin systems, with Ising-like OOP elements connected by IP elements, can be created. Examples with the OOP elements arranged on a square and a kagome lattice are given in Figs. 3, H and I, respectively. The correlated Ising-like moments lead to the spontaneous formation of domains with antiferromagnetic ordering for the square lattice and frustrated behavior for the kagome lattice with highly degenerate low energy states.

Another interesting application concerns the current-induced switching of magnetic elements, which is a basic requirement for the all-electrical operation of integrated nonvolatile magnetic memory and logic devices. Our measurements show that the OOP and IP regions can be simultaneously switched by an electric current flowing in the Pt/Co layer orthogonal to the IP magnetization (Fig. 4). The switching is caused by the current-induced spin-orbit torques that originate from the spin Hall and interface effects found in ferromagnets adjacent to heavy metal layers (*28-31*). Such electrical switching cannot be implemented in dipolar-coupled magnetic elements, which are usually too thick to be manipulated by spin torques. Moreover, the chiral coupling enables entirely field-free switching of the OOP magnetization*32-36*). In Fig. 4B, we show that the OOP region switches deterministically in zero field for a current I_{SW} = 5 mA injected parallel to *x*. Applying a field H_{ext} // ±*y* along the IP easy axis leads to a decrease or

increase of the switching current, which is proportional to H_{ext} (Fig. 4C). We interpret this behavior as the field assisting or counteracting the reversal of the IP magnetization that is driven by the damping-like component of the spin-orbit torque. This suggests that the current drives the switching of the IP magnetization (*30*,*37*), and that the reversal of the OOP region is a consequence of the chiral coupling. As the current density required to switch the IP magnetization is typically lower than that required by the OOP magnetization (*37*, *38* and Fig. S5C), OOP-IP coupled structures offer an efficient and scalable approach to field-free switching of magnetic devices, which is furthermore compatible with the materials and processes currently employed in the fabrication of magnetic memories.

Coupled OOP-IP building blocks demonstrated here can be used to fabricate synthetic antiferromagnets with linear and curved geometries, synthetic skyrmions, and artificial spin ices. Indeed, the spontaneous formation of the ground state following magnetization in an athermal artificial spin ice network reflects the strong nearest neighbor interactions in these systems, which is likely to lead to interesting frustrated behavior. Furthermore, the multiplicity of magnetic states that can be stabilized in OOP-IP elements combined with all-electric synchronous switching opens a route for the realization of nanomagnet logic gates and memory devices as well as for the design of electrically reconfigurable magnonic crystals, which can be used to manipulate the propagation of spin waves in synthetic media or provide a controlled modulation of the magnetic stray field in hybrid materials, such as ferromagnet/semiconductor and ferromagnet/superconductor heterostructures.

References and Notes:

1. P. Grünberg, R. Schreiber, Y. Pang, M. B. Brodsky, H. Sowers, Layered magnetic structures: evidence for

antiferromagnetic coupling of Fe layers across Cr interlayers. *Phys. Rev. Lett.* ***57***, 2442 (1986).

2. S. S. Parkin, N. More, K. P. Roche, Oscillations in exchange coupling and magnetoresistance in metallic superlattice structures: Co/Ru, Co/Cr, and Fe/Cr. *Phys. Rev. Lett.* ***64***, 2304 (1990).

3. R. A. Duine, K. J. Lee, S. S. Parkin, M. D. Stiles, Synthetic antiferromagnetic spintronics. *Nat. Phys.* ***14***, 217 (2018).

4. M. N. Baibich et al., Giant magnetoresistance of (001) Fe/(001) Cr magnetic superlattices. *Phys. Rev. Lett.* ***61***, 2472 (1988).

5. G. Binasch, P. Grünberg, F. Saurenbach, W. Zinn, Enhanced magnetoresistance in layered magnetic structures with antiferromagnetic interlayer exchange. *Phys. Rev. B* ***39***, 4828 (1989).

6. J. Nogués, I. K. Schuller, Exchange bias. *J. Magn. Magn. Mater.* ***192***, 203-232 (1999).

7. B. Dieny et al., Giant magnetoresistive in soft ferromagnetic multilayers. *Phys. Rev. B* ***43***, 1297 (1991).

8. S. S. Parkin et al., Exchange-biased magnetic tunnel junctions and application to nonvolatile magnetic random access memory. *J. Appl. Phys.* ***85***, 5828 (1999).

9. R. P. Cowburn, M. E. Welland, Room temperature magnetic quantum cellular automata. *Science* ***287***, 1466 (2000).

10. A. Imre et al., Majority logic gate for magnetic quantum-dot cellular automata. *Science* ***311***, 205 (2006).

11. R. F. Wang et al., Artificial 'spin ice' in a geometrically frustrated lattice of nanoscale ferromagnetic islands. *Nature* ***439***, 303 (2006).

12. L. J. Heyderman, R. L. Stamps, Artificial ferroic systems: novel functionality from structure, interactions and dynamics. *J. Phys. Condens. Matter.* ***25***, 363201 (2013).

13. I. Dzyaloshinsky, A thermodynamic theory of "weak" ferromagnetism of antiferromagnetics. *J. Phys. Chem. Solids* ***4***, 241 (1958).

14. T. Moriya, Anisotropic superexchange interaction and weak ferromagnetism. *Phys. Rev.* ***120***, 91 (1960).

15. M. Bode et al., Chiral magnetic order at surfaces driven by inversion asymmetry. *Nature* ***447***, 190 (2007).

16. S. Heinze et al., Spontaneous atomic-scale magnetic skyrmion lattice in two dimensions. *Nat. Phys.* ***7***, 713 (2011).

17. A. Fert, N. Reyren, V. Cros, Magnetic skyrmions: advances in physics and potential applications. *Nat. Rev. Mater.* ***2***, 17031 (2017).

18. M. Heide, G. Bihlmayer, S. Blügel, Dzyaloshinskii-Moriya interaction accounting for the orientation of magnetic domains in ultrathin films: Fe/W (110). *Phys. Rev. B* ***78***, 140403 (2008).

19. J. P. Tetienne et al., The nature of domain walls in ultrathin ferromagnets revealed by scanning nanomagnetometry. *Nat. Commun.* ***6***, 6733 (2015).

20. A. Thiaville, S. Rohart, E. Jue, V. Cros, A. Fert, Dynamics of Dzyaloshinskii domain walls in ultrathin magnetic films. *Eur. Phys. Lett.* ***100***, 57002 (2012).

21. S. Emori, U. Bauer, S. M. Ahn, E. Martinez, G. S. Beach, Current-driven dynamics of chiral ferromagnetic domain walls. *Nat. Mater.* ***12***, 611 (2013).

22. K. S. Ryu, L. Thomas, S. H. Yang, S. S. Parkin, Chiral spin torque at magnetic domain walls. *Nat. Nano.* ***8***, 527 (2013).

23. F. C. Ummelen, H. J. Swagten, B. Koopmans, Racetrack memory based on in-plane-field controlled domain-wall pinning. *Sci. Rep.* ***7***, 833 (2017).

24. Materials and methods are available as supplementary materials.

25. M. Belmeguenai et al., Interfacial Dzyaloshinskii-Moriya interaction in perpendicularly magnetized Pt/Co/AlOx ultrathin films measured by Brillouin light spectroscopy. *Phys. Rev. B* ***91***, 180405 (2015).

26. H. Yang, A. Thiaville, S. Rohart, A. Fert, M. Chshiev, Anatomy of Dzyaloshinskii-Moriya interaction at Co/Pt interfaces. *Phys. Rev. Lett.* ***115***, 267210 (2015).

27. S. Monso et al., Crossover from in-plane to perpendicular anisotropy in Pt/CoFe/AlOx sandwiches as a function of Al oxidation: A very accurate control of the oxidation of tunnel barriers. *Appl. Phys. Lett.* ***80***, 4157 (2002).

28. I. M. Miron et al., Perpendicular switching of a single ferromagnetic layer induced by in-plane current injection. *Nature* ***476***, 189 (2011).

29. M. Baumgartner et al., Spatially and time-resolved magnetization dynamics driven by spin–orbit torques. *Nat. Nano.* ***12***, 980 (2017).

30. L. Liu et al., Spin-torque switching with the giant spin Hall effect of tantalum. *Science* ***336***, 555 (2012).

31. K. Garello et al., P., Symmetry and magnitude of spin–orbit torques in ferromagnetic heterostructures. *Nat. Nano.* ***8***, 587 (2013).

32. G. Yu et al., Switching of perpendicular magnetization by spin–orbit torques in the absence of external

magnetic fields. *Nat. Nano.* ***9***, 548 (2014).

33. S. Fukami, C. Zhang, S. DuttaGupta, A. Kurenkov, H. Ohno, Magnetization switching by spin–orbit torque in an antiferromagnet–ferromagnet bilayer system. *Nat. Mater.* ***15***, 535 (2016).

34. Y. W. Oh et al., Field-free switching of perpendicular magnetization through spin–orbit torque in antiferromagnet/ferromagnet/oxide structures. *Nat. Nano.* ***11***, 878 (2016).

35. A. van den Brink et al., Field-free magnetization reversal by spin-Hall effect and exchange bias. *Nat. Commun.* ***7***, 10854 (2016).

36. K. Cai et al., Electric field control of deterministic current-induced magnetization switching in a hybrid ferromagnetic/ferroelectric structure. *Nat. Mater.* ***16***, 712 (2017).

37. S. Fukami, T. Anekawa, C. Zhang, H. Ohno, A spin–orbit torque switching scheme with collinear magnetic easy axis and current configuration. *Nat. Nano.* ***11***, 621 (2016).

38. K. S. Lee, S. W. Lee, B. C. Min, K. J. Lee, Threshold current for switching of a perpendicular magnetic layer induced by spin Hall effect. *Appl. Phys. Lett.* ***102***, 112410 (2013).

Acknowledgments: We thank A. Weber, H. Arava and V. Guzenko for technical support with sample fabrication. **Funding:** This work was supported by the Swiss National Science Foundation through grants No. 200021-153540, 200020-172775, and 200021-160186. J.C. has received funding from the European Union's Horizon 2020 research and innovation program under the Marie Skłodowska-Curie grant agreement No. 701647. **Author contributions:** This work is a partnership that was led jointly and equally by the L.H. and P.G. groups. Z.L., T.P.D., L.H., and P.G. conceived the work and designed the experiments; Z.L. fabricated the samples and performed the electrical measurements with the support of T.P.D. and E.K.; Z.L. analyzed and interpreted the data from the electrical measurements with the help of T.P.D. and P.G.; Z.L., J.V., A.K., T.P.D., J.C., M.B., T.S., and G.K. performed the XPEEM measurements, which were interpreted by Z.L., J.V. and A.K.; A.H. performed the micromagnetic simulations; Z.L., P.G., and L.H. worked on the manuscript together; All authors contributed to the discussion of the results and the manuscript revision. **Competing interests:** Authors declare no competing interests. **Data and materials availability:** All data used in this Report has been deposited in the Zenodo public database. The micromagnetic simulations were performed using the open source code mumax[3].

Supplementary Materials:

Materials and Methods

Supplementary Text

Figures S1-S15

Figures and figure legends:

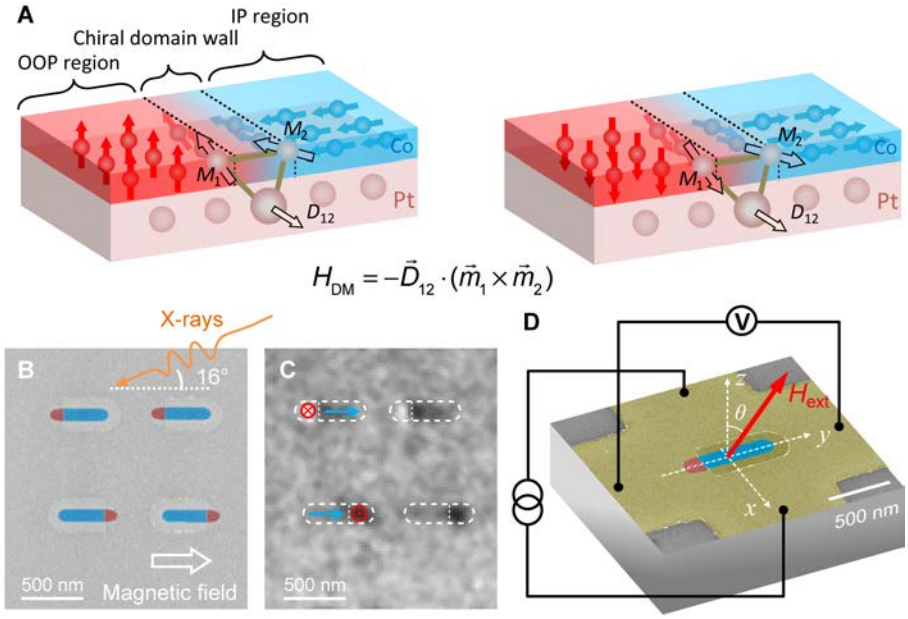

Fig. 1. Chiral coupling between OOP and IP magnets. (**A**) Schematics of the coupled magnetization states favored by the DMI in adjacent OOP and IP regions of a Pt/Co/AlO_x trilayer. (**B**) Scanning electron micrograph of coupled OOP-IP elements fabricated by electron-beam lithography. Red and blue colors indicate regions with OOP and IP magnetization, respectively. (**C**) X-PEEM image with bright and dark magnetic contrast in the OOP regions corresponding to ↓ and ↑ magnetization, respectively. The dark gray contrast in the IP regions corresponds to → magnetization. The direction of the incident x-rays and the in-plane magnetic field used for pre-alignment are indicated by arrows. (**D**) Schematic of an OOP-IP element fabricated on top of a Hall cross for electric measurements.

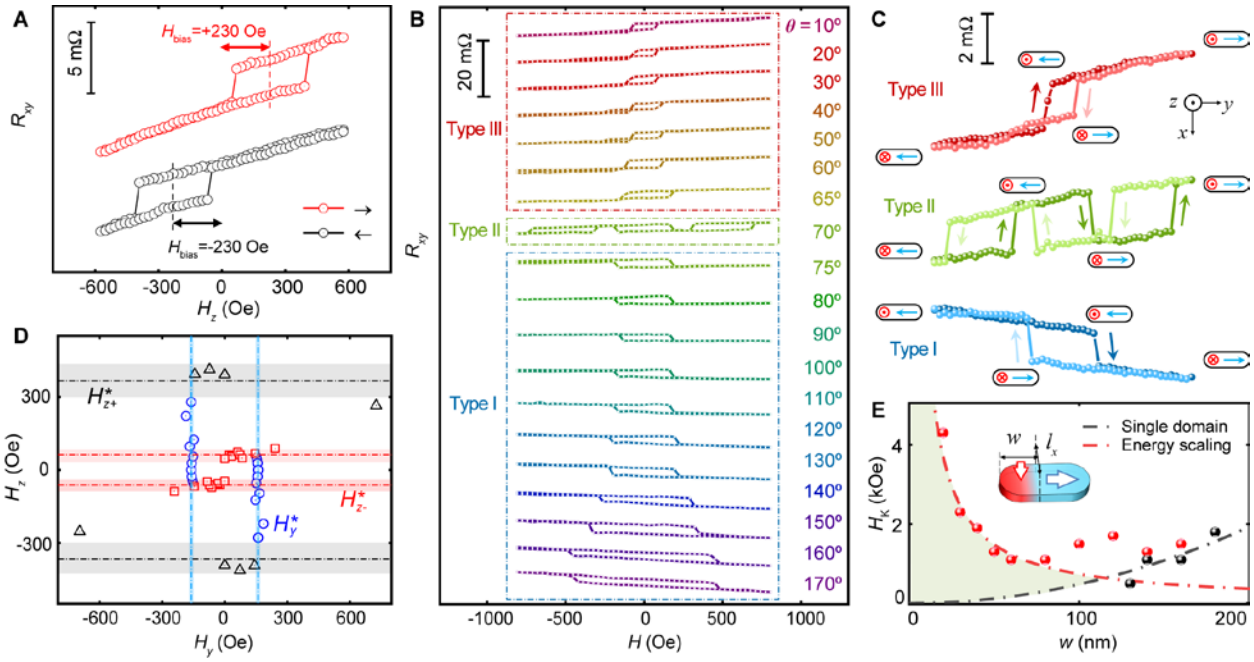
A
5 mΩ
H_{bias}=+230 Oe
H_{bias}=-230 Oe
R_{xy}
H_z (Oe)
B
20 mΩ
Type III
Type II
Type I
θ = 10°
20°
30°
40°
50°
60°
65°
70°
75°
80°
90°
100°
110°
120°
130°
140°
150°
160°
170°
R_{xy}
H (Oe)
C
2 mΩ
Type III
Type II
Type I
z
y
x
D
H^*_{z+}
H^*_{z-}
H^*_y
H_z (Oe)
H_y (Oe)
E
Single domain
Energy scaling
w
l_x
H_K (kOe)
w (nm)

Fig. 2. Exchange bias and field-induced switching of chirally-coupled OOP-IP elements. (**A**) OOP magnetization as a function of H_z for the OOP-IP element shown in Fig. 1D for right and left orientation of the magnetization in the IP region. The hysteretic jumps of the anomalous Hall resistance R_{xy} indicate switching of the OOP magnetization. The linear increase of R_{xy} with field is caused by the gradual tilt of the IP magnetization towards the *z* axis. (**B**) Magnetic hysteresis loops for a magnetic field tilted in the *y*-*z* plane for various tilt angles theta. (**C**) Multistate switching configurations I, II, and III corresponding to the hysteresis loops for θ = 30°, 70° and 140° shown in B. (**D**) Critical switching field H^*_{z+} (black triangles), H^*_{z-} (red squares), and H^*_y (blue circles) of the OOP region. The lines are fits according to the macrospin model described in the text with errors indicated by the shaded regions. (**E**) Boundaries of the single domain behavior (black line) and chiral-coupling (red line) as a function of the OOP magnetic anisotropy field H_K and element size *w*. The red and black points are determined from micromagnetic simulations. The shaded area indicates the range of parameters for which chiral coupling determines the magnetic configuration.

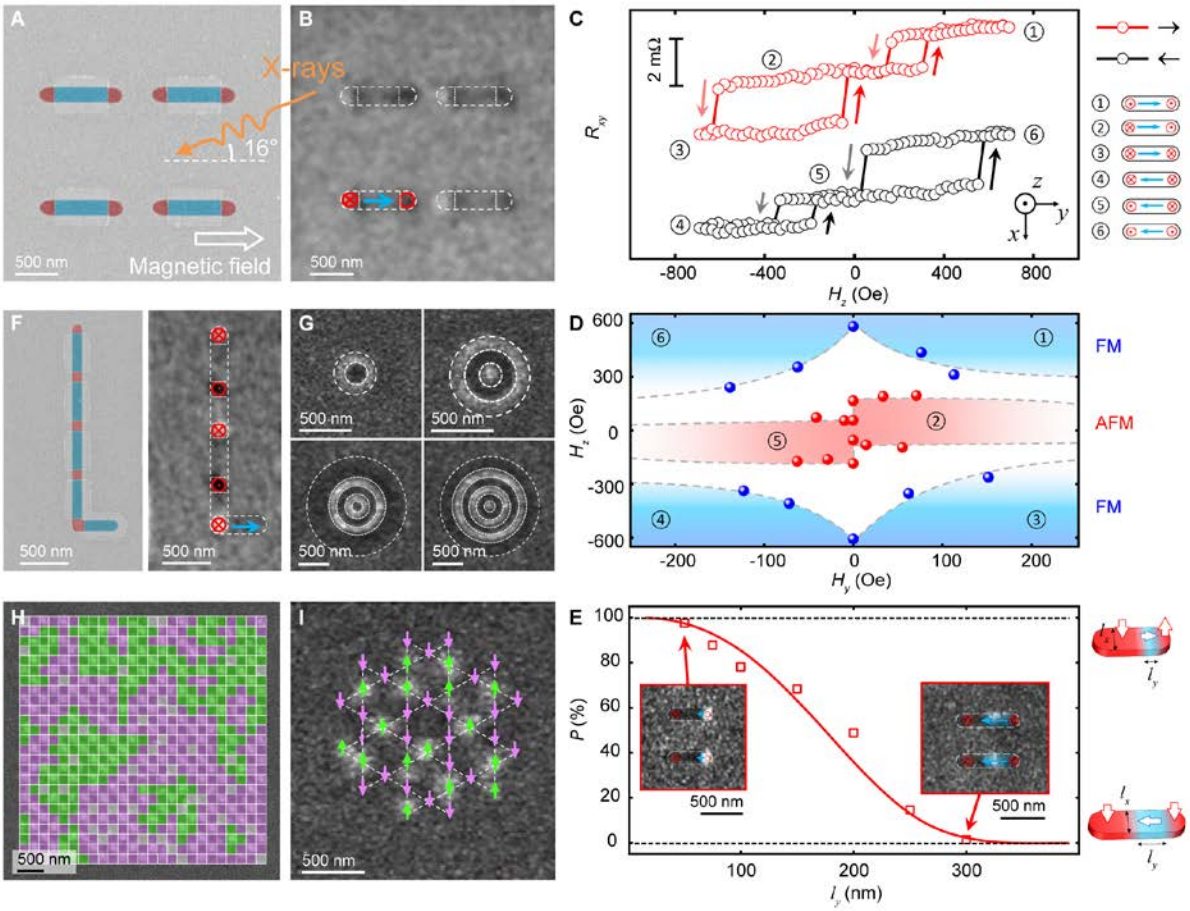

Fig. 3. Lateral synthetic antiferromagnets based on chiral coupling. (**A**) Scanning electron micrograph of coupled OOP-IP-OOP elements and (**B**) corresponding X-PEEM image. The stable magnetic configuration of the OOP-IP-OOP element is ↓ → ↑ after pre-alignment of the central region with an in-plane field pointing to the right. (**C**) Magnetic hysteresis of an OOP-IP-OOP element as a function of H_z for two opposite orientations of the IP spacer. The six possible magnetic configurations are shown. (**D**) H_z *vs* H_y phase diagram of the OOP-IP-OOP element used for (C). The red (blue) dots are the critical fields delimiting the antiferromagnetic (ferromagnetic) alignment of the two OOP regions. In the white shaded area, the configuration depends on the history of the magnetization. (**E**) Probability of correlated switching resulting in antiferromagnetically aligned OOP regions as a function of the length l_y of the IP spacer.

Saturating fields are applied, first -H_y and then -H_z, before applying a field H_z and measuring the magnetic state of the element. Each data point is averaged over 41 different elements. Insets: MFM images of OOP-IP-OOP elements with l_y =50 nm and 300 nm. The bright and dark MFM contrast corresponds to ↑ and ↓ magnetizations, respectively. (**F**) Scanning electron micrograph and X-PEEM image of a chain structure including five OOP regions, which align antiparallel after a field has been applied perpendicular to the chain (parallel to the lowest IP region). (**G**) MFM images of synthetic skyrmions with 1, 2, 4, and 5 IP rings after saturation by a magnetic field -H_z. (**H**) MFM image of an artificial spin system consisting of OOP elements acting as Ising-like moments coupled via IP spacers after saturating with a magnetic field -H_z. Antiferromagnetic domains are shaded in green and purple. (**I**) MFM image of an artificial kagome spin system after saturating with a magnetic field -H_z. The green and purple arrows indicate the orientation of the magnetization of the OOP vertices. All XPEEM and MFM images have been recorded at zero field.

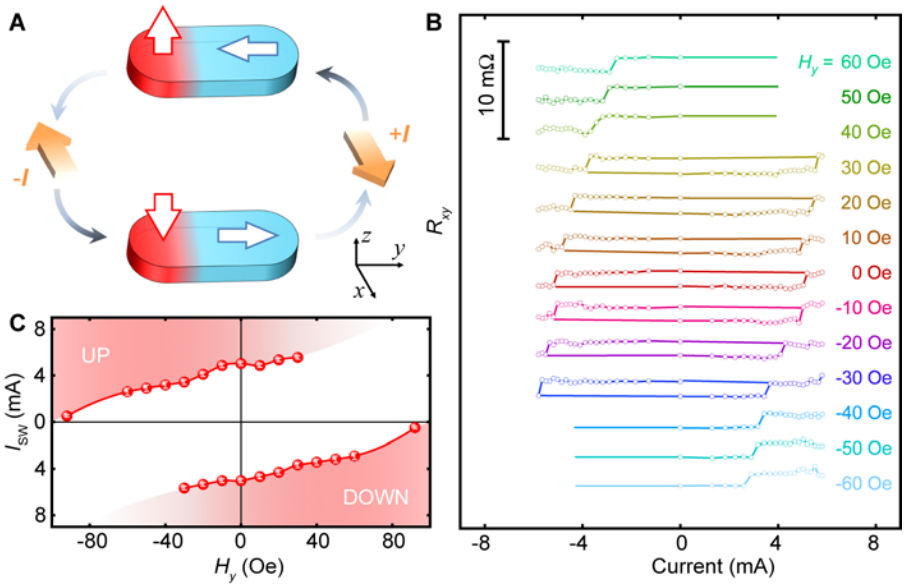

Fig. 4. Field-free current-induced magnetization switching of OOP-IP elements. (**A**) Schematics of the current-induced switching of an OOP-IP element. The device geometry is shown in Fig. 1D, the area of the OOP region is about 120 nm x 120 nm. (**B**) Magnetization loops as a function of applied current for different values of H_y. The measurements are performed by injecting 50 μs long current pulses and measuring the anomalous Hall resistance R_{xy} after each pulse. Changes in R_{xy} indicate switching of the OOP region. The switching at zero field is symmetric with respect to the current, whereas $H_y>0$ helps to switch the OOP region ↓and decrease the negative switching current and $H_y<0$ helps to switch the OOP region ↑ and decrease the positive switching current. (**C**) Critical switching current I_{SW} as a function of H_y. The range of parameters leading to deterministic switching between ↑ and ↓ states is shaded in red.